ROYAL SOCIETY OF CHEMISTRY

PAPER

Check for updates

Sequential delivery of synergistic drugs by silica nanocarriers for enhanced tumour treatment†

Albane Birault,[a] Simon Giret,[a] Christophe Théron,[a] Audrey Gallud,[b] Afitz Da Silva,[b] Denis Durand,[b] Christophe Nguyen, [ID][b] Nadir Bettache, [ID][b] Magali Gary-Bobo, [ID][b] John R. Bartlett, [ID][cd] Michel Wong Chi Man [ID][a] and Carole Carcel [ID]*[a]

Herein hybrid silica nanoparticles have been engineered to direct the sequential delivery of multiple chemotherapeutic drugs in response to external stimuli such as variations in pH. The nanocarriers consist of conventional MCM-41-type nanoparticles, which have been functionalised with an organic ligand (or stalk) grafted onto the external surface. The stalk is designed to "recognise" a complementary molecule, which serves as a "cap" to block the pores of the nanoparticles. First, camptothecin is introduced into the pores by diffusion prior to capping the pore apertures *via* molecular recognition. The cap, which is a derivative of 5-fluorouracil, serves as a second cytotoxic drug for synergistic chemotherapy. *In vitro* tests revealed that negligible release of the drugs occurred at pH 7.4, thus avoiding toxic side effects in the blood stream. In contrast, the stalk/cap complex is destabilised within the endolysosomal compartment (pH 5.5) of cancer cells, where release of the drugs was demonstrated. Furthermore, this environmentally responsive system exhibited a synergistic effect of the two drugs, where the pH-triggered release of the cytotoxic cap followed by diffusion-controlled release of the drug cargo within the pores led to essentially complete elimination of breast cancer cells.

Introduction

Combinatorial chemotherapy is widely employed as a primary treatment approach in cancer therapy to overcome the easily-developed defence of cancer cells against a single drug.[1,2] However, conventional therapies involving the use of multiple free drugs often lead to well-known severe toxic side effects.[2,3] One of the most effective approaches for overcoming such limitations is to load multiple therapeutic agents that exploit different anti-tumour mechanisms into a single effective nano-carrier with no drug leakage before reaching the target. Such smart nanocarriers could then increase the therapeutic efficiency and reduce toxic side effects by improving the bio-accessibility of drugs.[4–8] In this sense, mesoporous silica nanoparticles (MSNPs) have been widely used, due to their versatility in forming the basis of stimuli-responsive drug delivery systems.[9–13]

Notably, pH-responsive MSNPs provide the advantage of being endogenously stimulated due to the difference in pH between cellular compartments.[14–16] We recently reported[17] the use of molecular recognition *via* H-bonding to design smart silica nanoparticles with a pH-activated cap, which exhibited slow release kinetics under slightly acidic conditions and good efficacy for cancer cells elimination.

In order to avoid the well-known phenomenon of anti-cancer drug resistance and to optimize this earlier nanosystem, the current work explored the design of a multi-drug nanoplatform for combined chemotherapy. Our strategy, outlined in Scheme 1, involves coupling silica nanocarriers embodying molecular recognition sites with an active cap to enhance the anti-tumour activity.

After loading the functionalised nanoparticles with camptothecin (CPT, **Drug 1**), the pores are closed to avoid premature release under physiological conditions within the bloodstream (pH 7.4) using a 5-fluorouracil (5-FU) derivative (**Drug 2**), which can create stable H-bonds with **Stalk** located on the nanoparticles' surfaces. The opening of the pores is then triggered at the acidic pH within lysosomes (pH 4.5–5.5), to deliver sequentially the two drugs within the cancer cells because of **Stalk** protonation followed by disruption of the **Stalk–Cap** bonds.

As already mentioned, there are a plethora of studies reporting MSNPs' efficacy for cancer therapy applications.[18,19] Although some of these have described the use of drugs as pore-blockers

[a] *ICGM, Univ. Montpellier, CNRS, ENSCM, Montpellier, France.*
  E-mail: carole.carcel@enscm.fr
[b] *Institut des Biomolécules Max Mousseron, UMR5247, Université de Montpellier, CNRS, ENSCM, Faculté de Pharmacie, 15 avenue Charles Flahault, 34093, Montpellier, Cedex 05, France*
[c] *University of the Sunshine Coast, 90 Sippy Downs Drive, Sippy Downs QLD 4556, Australia*
[d] *Western Sydney University, Locked Bag 1797, Penrith, NSW, 2751, Australia*
† Electronic supplementary information (ESI) available. See DOI: 10.1039/c9tb02225b
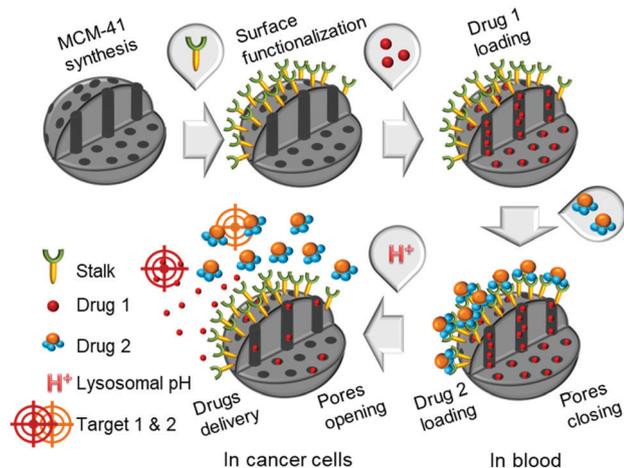
Scheme 1 Conceptual combinatorial drug delivery MSNP nanocarriers with **Drug 1** (camptothecin) encapsulated inside the pores and **Drug 2** (5-FU derivative) as the capping agent.
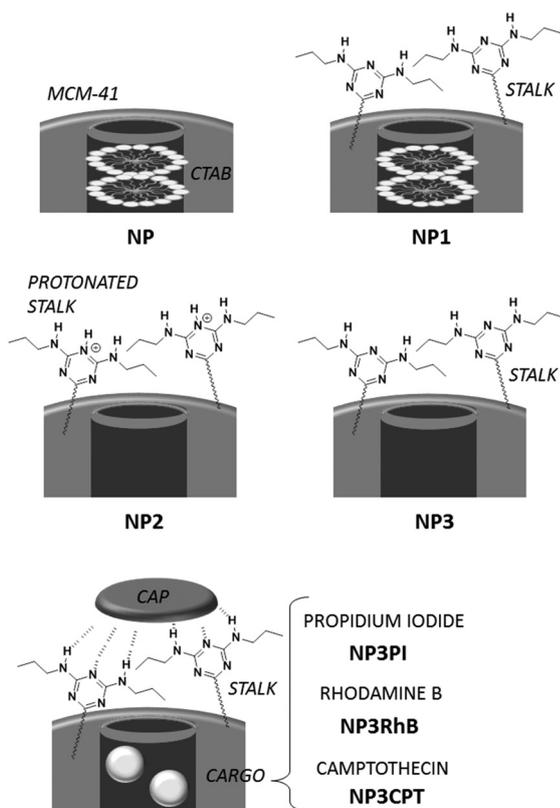
Scheme 2 Synthesis of capped nanoparticles.

to form promising nanocarriers for combination therapy,[20–22] to the best of our knowledge, this is the first time that a pH-responsive nanocarrier has been employed to exploit the synergistic toxicity of combining CPT and 5-FU for anti-cancer drug resistance applications.

To develop such systems, two separate syntheses are required: (1) the functionalisation of appropriate silica nanocarriers such as MCM-41, by **Stalk** grafting, to provide selective H-bonding

recognition sites on the external surface; and (2) the synthesis of an antitumor derivative, with a complementary molecular recognition pattern, which, by pairing with the corresponding **Stalks**, would then cap the pores.

Organosilylated triazine derivatives, bearing donor–acceptor–donor recognition sites, were used as **Stalks** condensed onto the surface of the nanoparticles. The **Stalk** employed in this study is tetrasilylated, which enhances the functionality of the platform by providing additional degrees of freedom and binding sites for grafting the ligand onto the surface of the nanoparticles, compared to our previously described bisilylated system.[17] The additional conformational flexibility of the tetrasilylated **Stalk** would also be expected to enable the amine sites on the ligand to orient correctly to form the desired H-bonds with the **Cap**. As drug candidates, we chose for the pore-blocker a commonly used anticancer drug, 5-fluorouracil (5-FU), which exhibits complementary molecular recognition properties to **Stalk**. Previously,[23] we have demonstrated that a derivative such as **Cap** (Fig. 1) with a three-fold H-bonding pattern favours stable complexation at neutral pH in bulk hybrid silica materials. In contrast, the complex begins to dissociate at lower pH after triazine unit protonation, leading to the breakdown of H-bonds initially involved in stabilization of the capping complex, thus promoting removal of **Cap** at pH 5.5 and below and its associated release. The biological activity of **Cap** was previously evaluated[23] by cytotoxic assay on MCF-7 human breast cancer cells, showing a relatively high efficiency (43% of breast cancer cell death at 50 μM) for this molecule as an anticancer drug compared with the parent 5-FU (68% of cell death at 50 μM).

To investigate their viability and the combination therapeutic effect, we evaluated the cytotoxicity of these MSNPs towards human breast cancer cells (MCF-7). In a first study, the functionalised nanoparticles were loaded with fluorescent dyes, such as propidium iodide (PI) or rhodamine-B (RhB), to validate the opening of the pores in weakly-acidic lysosomal media and to assess the internalization of the MSNPs in the cells. In a second
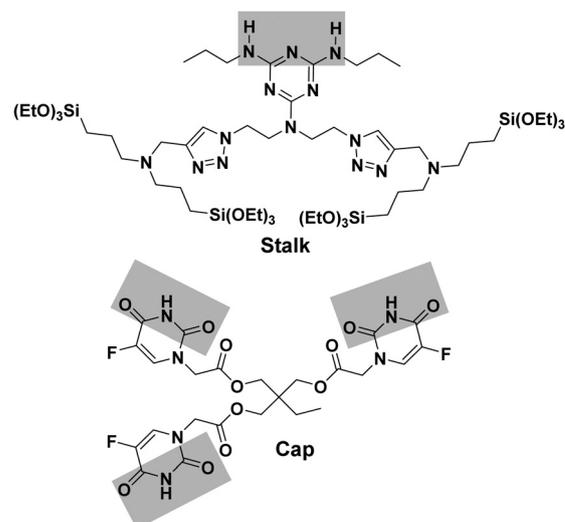

Fig. 1 Structures of **Stalk** precursor and **Cap**.

This journal is © The Royal Society of Chemistry 2020

J. Mater. Chem. B, 2020, **8**, 1472–1480 | **1473**

study, the MSNPs were loaded with CPT and the pores capped with 5-FU derivative **Cap** to examine the overall cytotoxicity by *in vitro* studies. CPT destroys cancer cells *via* a different biological pathway than 5-FU[24,25] and the two drugs have been previously shown to demonstrate a strong synergistic effect when used together to treat cancer cells.[26] The approach outlined in this study enables two cytotoxic drugs to be delivered autonomously and sequentially, which is typically the manner in which injection- or drip-based combination drug therapies are administered to maximise the efficacy of such treatment. Under *in vitro* conditions, the multi-drug payload is retained under normal physiological conditions and then released autonomously at the disease site, demonstrating nearly complete cell apoptosis within 72 h.

Experimental section

General

5-Fluorouracil, thionyl chloride, triethylamine and 1,1,1-tri-(hydroxymethyl)propane were purchased from Sigma, USA and were used without purification. Solvents were dried by employing a MB SPS-800 apparatus.

Characterization

FTIR spectra were obtained on a PerkinElmer FT-IR Spectrum BX spectrometer. CPMAS solid-state NMR spectra were obtained using a Bruker FT-AM 400 spectrometer and ^{1}H- and ^{13}C-NMR spectra were obtained using a Bruker AC-400 spectrometer, with CDCl$_3$ or DMSO-d$_6$ as solvent and tetramethylsilane (TMS) as a reference. N$_2$ adsorption/desorption isotherms were obtained using a Micromeritics ASAP 2010 instrument at 77.15 K. Specific surface areas were calculated using the BET transform directly from the isotherms, using 0.162 nm^2 as the cross-sectional area of N$_2$. Electron micrographs were obtained with a JEOL 1200 EXII microscope for TEM and with a Hitachi S4800 30 kV apparatus for the SEM data. ^{29}Si solid-state NMR spectra were obtained using a Bruker DSX 300 MHz spectrometer. Spectra were recorded using 4000 scans, with a relaxation delay of 3 s, pulse duration of 6 μs and acquisition time of 0.04 s.

Thermogravimetric analyses (TGA) were performed on a Netzsch TG 209 C apparatus employing a heating rate of 10 °C min^{-1} under an air flow of 20 mL min^{-1} up to 585 °C. The small and wide-angle X-ray scattering (SWAXS) experiments were conducted using a Guinier Mering set up with a 2D image plate detector.

Precursor synthesis

Synthesis of 5-FUA. 5-FUA was prepared according to a previously reported method.[27] Yield: 54%; m.p. 274–276 °C.

^{1}H NMR (400 MHz, DMSO-d$_6$): δ = 11.93 (s, 1H), 8.09 (d, 1H), 4.37 ppm (s, 2H); ^{13}C NMR (100 MHz, DMSO-d$_6$, δ): δ = 168.6, 158.2, 150.8, 140.1, 128.2, 53.4; HRMS (ESI) *m/z*: [M + H]$^+$ calcd for C$_6$H$_6$N$_2$O$_4$F: 189.0312; found: 189.0313.

Synthesis of Cap (Fig. 2). The synthesis of **Cap** was adapted from a previously reported procedure.[22] **5-FUA** (1.1 g, 5.85 mmol) and triethylamine (126 μL, 0.904 mmol) were dissolved in dry
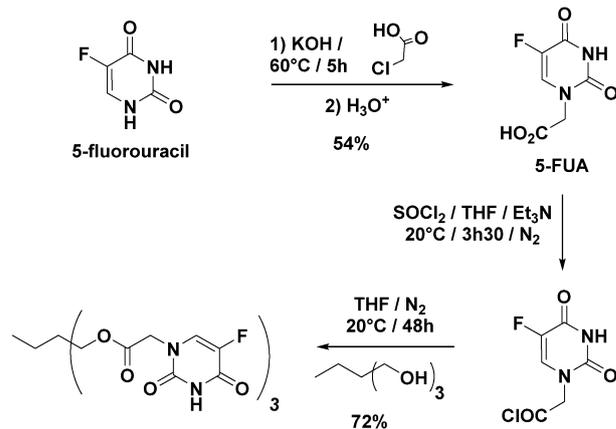
Fig. 2 Optimized synthesis of **Cap**.

THF (44 mL) and freshly distilled SOCl$_2$ (8.4 mL) at 20 °C under N$_2$. After 3.5 h, excess SOCl$_2$ and THF were removed under vacuum and the residue was re-dissolved in dry THF (42 mL). 1,1,1-Tri(hydroxymethyl)propane (80 mg, 0.60 mmol) was added and the mixture was stirred at 20 °C for 48 h. The solvent was then evaporated, and the residue was purified by column chromatography (CH$_2$Cl$_2$/MeOH: 98 : 2 90 : 10). Yield: 72%; m.p. decomposition after 180 °C.

^{1}H NMR (400 MHz, DMSO-d$_6$): δ = 12.00 (s, 3H), 8.04 (d, 3H), 4.50 (s, 6H), 4.05 (s, 6H), 1.36 (q, 2H), 0.79 ppm (t, 3H); ^{13}C NMR (100 MHz, DMSO-d$_6$): δ = 20.9, 34.7, 48.7, 63.4, 130.1, 138.1, 140.5, 149.6, 157.2, 167.6 ppm; HRMS (ESI) *m/z*: [M + H]$^+$ calcd for C$_{24}$H$_{24}$N$_6$O$_{12}$F$_3$: 645.1404; found: 645.1412.

Synthesis of Stalk (Fig. 3). The **Stalk** was prepared according to a previously reported procedure.[28] Firstly, compound **1** was added dropwise (due to its potentially-explosive nature, care
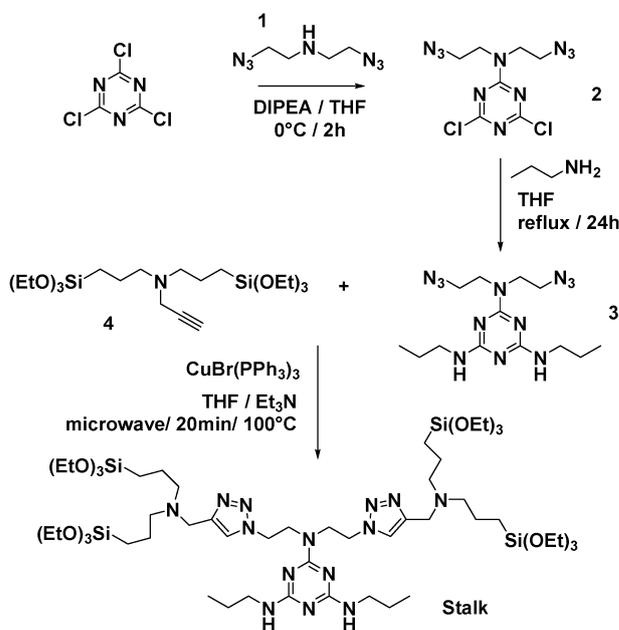
Fig. 3 Synthesis of **Stalk**.

should be taken) to a solution of cyanuric chloride in THF in the presence of *N,N*-diisopropylethylamine (DIPEA) at 0 °C, to afford **2** (66% yield). Compound **2** was then dissolved in THF with 10 equivalents of propylamine under reflux to give **3** (90% yield). Finally, the tetrasilylated **Stalk** was obtained *via* a CuAAC Click coupling reaction between **3** and **4**. The reagents were introduced into a microwave oven in the presence of the CuBr(PPh$_3$)$_3$ catalyst and Et$_3$N in THF at 100 °C for 20 minutes to yield the **Stalk** (Fig. S1, ESI†) in quantitative yield.

^{1}H NMR (400 MHz, CDCl$_3$, Fig. S1, ESI†): δ = 0.56 (t, 8H), 0.95 (t, 6H), 1.22 (t, 36H), 1.58 (m, 12H), 2.39 (t, 8H), 3.29 (q, 4H), 3.64 (m, 8H), 3.80 (q, 24H), 4.47 (t, 4H), and 7.32 (s, 2H). ^{13}C NMR (100 MHz, CDCl$_3$): δ = 7.86 (s), 11.50 (s), 18.28 (s), 20.26 (s), 23.05 (s), 42.47 (s), 45.90 (s), 48.16 (s), 48.60 (s), 56.46 (s), 58.29 (s), 123.11 (s), 128.51 (s), and 132.01 (s). HRMS (ESI) *m/z*: [M + H]$^+$ calcd for C$_{55}$H$_{115}$N$_{14}$O$_{12}$Si$_4$ (MH): 1275.7896; found: 1275.7910.

Nanoparticles preparation (Scheme 2)

Synthesis of NP. Cetyltrimethylammonium bromide (CTAB; 315 mg, 8.6 × 10^{-1} mmol), was dissolved in Milli Q H$_2$O (150 mL, 8.3 × 10^3 mmol), and the pH was adjusted to ~12 by addition of NaOH solution (2 M, 1.1 mL). After heating the resulting solution to 80 °C, tetraethylorthosilicate (TEOS; 1.4 mL, 6.3 mmol) was added dropwise and the reaction was continued for 2 h to yield MCM-41 nanoparticles. Finally, the nanoparticles were collected after centrifugation and washing with EtOH. ^{29}Si CPMAS solid-state NMR: δ = −99.2, −108.9 ppm.

Synthesis of NP1. Stalk (80 mg, 0.10 mmol) was added to a suspension of MCM-41 (80 mg) (pre-heated overnight at 90 °C to remove traces of H$_2$O and to activate Si–OH functions) in dry toluene (10 mL) under an inert atmosphere. The suspension was then heated at 80 °C for 24 h, prior to centrifuging the nanoparticles and washing them twice with ethanol and then five times with water. ^{29}Si CPMAS NMR: δ = −57.4, −100.1, −108.9 ppm.

Synthesis of NP2. The CTAB surfactant was removed by washing with a solution of HCl 37 wt% (1 mL) in ethanol (80 mL) under reflux overnight. The resulting **NP2** nanoparticles were washed twice with EtOH.

Synthesis of NP3. Excess HCl associated with the **NP2** nanoparticles was removed by washing the nanoparticles with freshly distilled Et$_3$N (1 mL, 7.2 mmol) in H$_2$O (10 mL, 5.6 × 10^2 mmol) for 48 h at 70 °C. The resulting **NP3** nanoparticles were then washed two times with H$_2$O and three times with EtOH.

Loading, capping and release

NP3 nanoparticles were suspended in a solution of cargo molecules as described below. The suspension was then sonicated for 20 min and stirred for 18 h to promote filling of the pores with the cargo molecules. To ensure retention of the drug, the pore apertures were capped by addition of **Cap** (3 mg; 4.7 × 10^{-3} mmol) and the suspension was stirred for an additional 48 h. After centrifugation, the particles were washed with DMSO around 5–6 times following by washing with water and EtOH.

NP3PI (5 mM): PI (45 mg, 6.7 × 10^{-2} mmol) in water (13.5 mL), and nanoparticles (90 mg).

NP3RhB (5 mM): RhB (32 mg, 6.7 × 10^{-2} mmol) in water (13.5 mL), and nanoparticles (90 mg).

NP3CPT (3 mM): CPT (15 mg, 4.3 × 10^{-2} mmol) in DMSO (15 mL), and nanoparticles (90 mg).

The CPT loadings obtained under the conditions used to impregnate the **NP3** nanoparticles were 4 wt%, on the basis of visible absorbance spectroscopy studies.

The release of the CPT from **NP3CPT** mesopores was evaluated by UV-Vis absorbance at 380 nm at either pH 2, 5.5 or 7.4 for different periods of time over a 24 h period. For these studies, 3 mg of **NP3CPT** was dispersed into 1 mL of aqueous solution at the defined pH and then 100 µL aliquots of the nanoparticle dispersion were poured into Eppendorf tubes. The tubes were stirred during release of the drug and were then centrifuged (15 × 10^3 min^{-1}, 15 min). The resulting supernatant was placed into a microreader plate and the concentration of drug was determined from an appropriate calibration curve.

In vitro studies

Cell culture conditions. Human breast cancer cells (MCF-7) were purchased from ATCC (American Type Culture Collection, Manassas, VA). MCF-7 cells were cultured in DMEM-F12 culture medium supplemented with 10% foetal bovine serum and 50 µg mL^{-1} gentamycin. These cells were allowed to grow in a humidified atmosphere at 37 °C under 5% CO$_2$.

Cytotoxicity

MCF-7 cells were seeded into 96-well plates at 10^4 cells per well in 200 µL culture medium and allowed to grow for 24 h. The three batches of nanoparticles (**NP**, **NP3RhB**, and **NP3CPT**) were dispersed in ethanol at a concentration of 10^{-2} M and sonicated in an ultrasonic bath until completely dispersed. Then, cells were incubated for 72 h with different nanoparticle concentrations (from 1 to 100 µg mL^{-1}). For the **NP3CPT** batch, the experiment was also carried out for shorter lengths of time (6, 16 and 24 h). At the end of the incubation time, a MTT assay was performed to evaluate the toxicity. Briefly, cells were incubated for 4 h with 0.5 mg mL^{-1} of MTT (3-(4,5-dimethylthiazol-2-yl)-2,5-diphenyltetrazoliumbromide; Promega) in culture media. The MTT/media solution was then removed, and the precipitated crystals were dissolved in EtOH/DMSO (1:1). The solution absorbance was read at 540 nm.

Confocal imaging

MCF-7 cells were seeded one day prior to nanoparticle exposure at 10^6 cells per cm^2 in glass-bottomed culture dishes from Ibidi Biovalley®. Cells were then exposed for 20 h to 40 µg mL^{-1} of NPs. Prior to imaging, the cells were stained with 50 nM LysoTracker Green DND-26 for 30 min and 5 µg mL^{-1} Hoechst 33342 was added during the last 10 min of incubation. Confocal images were acquired on a Zeiss Axio Observer confocal microscope equipped with an oil-immersion Plan-Apochromat 63×/1.40 objective.

Flow cytometry

MCF-7 cells were seeded into a 6-well plate (Nunc; 10^6 cells per well) and allowed to grow for 24 h. The cells were harvested at 5, 18 and 22 h following NP exposure (40 µg mL^{-1}) and re-suspended in DMEM-F12 phenol red-free medium. Dead cells were counterstained with 4′,6-diamidino-2-phenylindole (DAPI, 0.5 µg mL^{-1}). The percentage of positive living cells for NP uptake was determined on a FACS Canto II flow cytometer. The data were analysed with Win MDI software v2.8.

Results and discussion

Preparation of precursors

The approach used to prepare the **Stalk** (Fig. 3 and Fig. S1, ESI†) was based on a previously reported method.[28]

Similarly, the **Cap** was prepared according to an optimised protocol based on a previously reported synthesis.[23] The reaction was performed in homogeneous medium and employed an eco-friendly room-temperature approach for the second and third steps, which led to an increased yield and a reduction in the overall reaction time (Fig. 2).

Nanoparticle synthesis, functionalisation, loading and capping

MCM-41 nanoparticles (**NP**) were prepared by classical sol–gel processing in alkaline aqueous solution. CTAB used to template the compact hexagonal porosity (Fig. S2, ESI†) in the MSNPs was retained in the pores, and the **Stalk** was then covalently grafted onto the MSNP surface by condensation. After washing with water, the resulting nanoparticles **NP1** were characterised by IR spectroscopy and solid-state ^{29}Si NMR to demonstrate successful functionalisation.

As shown in Fig. 4(A), bands arising from the **Stalk** in the spectrum of **NP1** are observed at 1557 and 1498 cm^{-1}, which are associated with –N=N and C=C stretching vibrations.[29] Notably, these vibrations are not evident in the corresponding **NP** spectrum. In the region from 2700 to 3100 cm^{-1} (Fig. 4(B)) the spectra of **NP** and **NP1** are similar and are dominated by bands associated with CTAB at 2854 and 2924 cm^{-1}. Hence the spectral features of **Stalk** are not clearly observed, except for a

shoulder at 2972 cm^{-1}. CTAB, initially retained within the pores to maximize functionalisation on the external surface, was then extracted with HCl to afford **NP2**. Excess HCl remaining after extraction of CTAB was neutralised by suspending **NP2** in an aqueous solution of Et$_3$N and stirring the resulting mixture for 48 h at 70 °C, before centrifugation and washing to give **NP3**. CTAB elimination was confirmed by the disappearance of its associated bands at 2854 and 2924 cm^{-1} in the IR spectrum of **NP3**. In addition, the loss of bands associated with **Stalk** ethoxy species at 1388 and 1439 cm^{-1} [30] in the spectrum of **NP3** (Fig. 4(A)) is consistent with successful grafting of Stalk onto the surface of **NP3**. Similarly, the decrease in the relative intensities of the **Stalk** bands at 2883 and 2972 cm^{-1}, which include contributions from $\nu_s(CH_3)$ and $\nu_{as}(CH_3)$, respectively, of ethoxy groups,[30] is consistent with loss of ethoxy species following grafting.

The solid-state ^{29}Si NMR spectrum of **NP1** (Fig. 5(B)) also demonstrated the successful grafting of the **Stalk**, with two sets of chemical shifts being evident. The first set, at −47, −57 and −67 ppm, are attributed to T^1, T^2 and T^3 sites, respectively, arising from the **Stalk** and are not observed in the spectrum of **NP** (Fig. 5(A)), as expected. The relatively high intensity of the T^2 signal compared to that of the T^3 signal indicates that condensation of the ethoxy/hydroxy species on the **Stalk** is
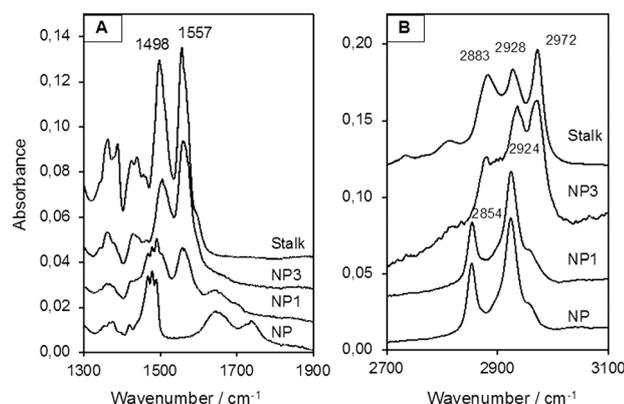

Fig. 4 IR spectra (A) from 1300 to 1900 cm^{-1} and (B) from 2700 to 3100 cm^{-1} of **NPs** and the **Stalk** precursor.
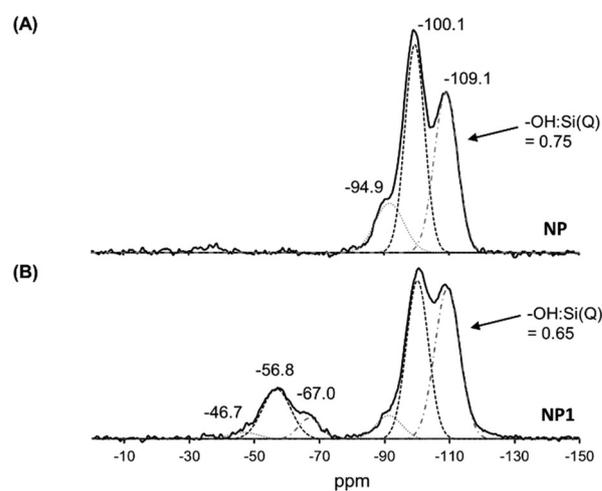

Fig. 5 Solid state ^{29}Si NMR spectra of **NP** (A) and **NP1** (B). (C) Isotherms of CTAB-free **NP**, **NP1** and **NP3** obtained by nitrogen sorption analyses.

1476 | *J. Mater. Chem. B*, 2020, **8**, 1472–1480

This journal is © The Royal Society of Chemistry 2020

incomplete after grafting, with some of the four Si sites in the grafted **Stalk** moieties being bound to the surface of the nanoparticles *via* two oxo bonds instead of three. The second set of peaks in the ^{29}Si-NMR spectra, at −95, −100 and −109 ppm, are assigned to Q^2, Q^3 and Q^4 species, respectively, within the MCM-41 framework. The increase in the relative intensity of the Q^4 signal for **NP1**, and the corresponding decrease in the −OH : Si ratio for the Q^n species following grafting (from 0.75 to 0.65), is associated with conversion of Q^2 and Q^3 species to Q^4 species during functionalisation. Thermogravimetric analysis (TGA) confirmed the presence of the organic **Stalk** on the surface of the MCM-41 nanoparticles (Fig. S3, ESI†).

The N_2 adsorption/desorption isotherms of **NP1** (grafted nanoparticles containing CTAB) are compared with those of CTAB-free **NP** and **NP3** in Fig. 5(C). As expected, **NP1** exhibits very low accessibility to small molecules such as N_2, with a corresponding BJH adsorption pore volume and BET surface area of 0.03 cm^3 g^{-1} and 21 m^2 g^{-1}, respectively, consistent with the presence of CTAB within the mesopores. In contrast, removal of CTAB by washing yields a mesoporous material (Type IV isotherm) with a pore volume of 0.92 cm^3 g^{-1} and BET surface area of 902 m^2 g^{-1}. The isotherm of CTAB-free **NP** shows a steep increase near $P/P_0 = 0.35$, consistent with the presence of ordered mesopores. The corresponding data for **NP3** are also consistent with a highly porous material, albeit with a smaller pore volume (0.72 cm^3 g^{-1}) and surface area (675 m^2 g^{-1}) than the unfunctionalised material **NP**. A slight increase in the adsorption branch at p/p_0 around 0.3 for **NP3** is consistent with smaller pore size than in the CTAB-free **NP**. More significantly, the isotherm of **NP3** has a distinct hysteresis with non-parallel branches on the adsorption and desorption arms. Such profiles are often observed for porous samples having ink-bottle type pores, consistent with modification of the external surface in the vicinity of the pore openings. These data suggest that functionalisation leads to some obstruction of the nanoparticle porosity, although the pore network is still highly accessible to small molecules such as N_2.

To load the functionalised nanoparticles with a drug cargo, **NP3** was suspended with several different cargos, including RhB, PI or CPT in water or DMSO. **Cap** was then added to the suspension to complex the **Stalks** on the surface and thus block the pores. The suspension was stirred at RT for a further 48 h and then centrifuged. The resulting nanoparticles were vigorously washed with DMSO (until a transparent supernatant was obtained) to remove adsorbed cargo that had not been incorporated within the pores prior to capping and residual physisorbed **Cap**. After additional washings with water and EtOH, the nanoparticles were dried under vacuum to give the **NP3RhB**, **NP3PI** or **NP3CPT** nanomaterials, depending on the cargo compound used.

The quantity of **Cap** complexed by **Stalk** in the **NP3** system was assessed by monitoring the relative quantities of Si, N and F in the **NP3CPT** system *via* energy dispersive X-ray (EDX)-TEM analysis. The results obtained are illustrated in Fig. 6 and Fig. S4 (ESI†). The semi-quantitative EDX analysis revealed significant quantities of F atoms (Fig. S4, ESI†) arising from
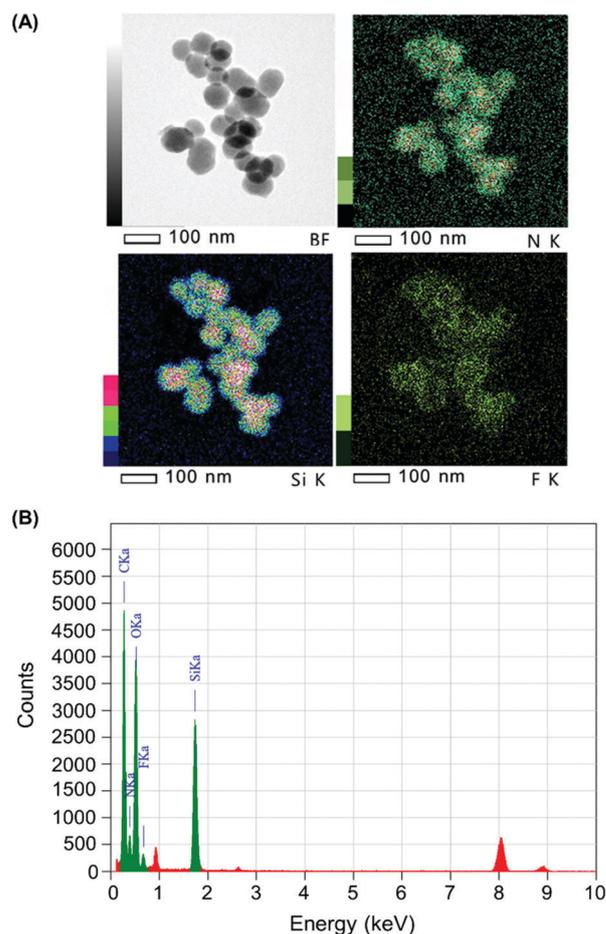

Fig. 6 (A) Bright field (BF) and elemental mapping (Si, N and F) and (B) EDX spectrum of **NP3CPT** by EDX-TEM.

the presence of surface-complexed **Cap**. In addition, the relative quantities of Si, N and F atoms (Fig. S4, ESI†), together with the relative masses of SiO_2 and **Stalk** determined by TGA (Fig. S3, ESI†), are consistent with a **Stalk** : **Cap** molar ratio of 3 : 1 and a CPT loading of 4.0 wt% in the **NP3CPT** system. The data also reveal the presence of three **Stalk** (and hence one **Cap**) per 100 Si atoms (see ESI†). This is consistent with the expected complexation between the complementary **Stalk** and **Cap** and the associated obstruction of the MSNP pore apertures in **NP3CPT**.

In addition, the size and morphology of the nanoparticles were characterized at different stages during the synthesis to verify their uniformity. SEM and TEM micrographs of **NP**, **NP3** and **NP3CPT** (Fig. 7A) showed relatively mono-dispersed nanoparticles with diameters ranging from 110 to 200 nm. The TEM images also revealed the expected transverse porosity in the materials. A comparison of the nanoparticle size obtained by SEM with that observed in solution *via* DLS studies (Fig. 7B) indicates that the functionalised nanoparticles are essentially unaggregated after being dispersed in solution, with relatively small polydispersity indices. As expected, the data indicate that functionalisation of **NP** with **Stalk**, to form **NP3**, results in a small increase in the hydrodynamic diameter of the nanoparticles (from 140 to ∼190 nm) without any increase in
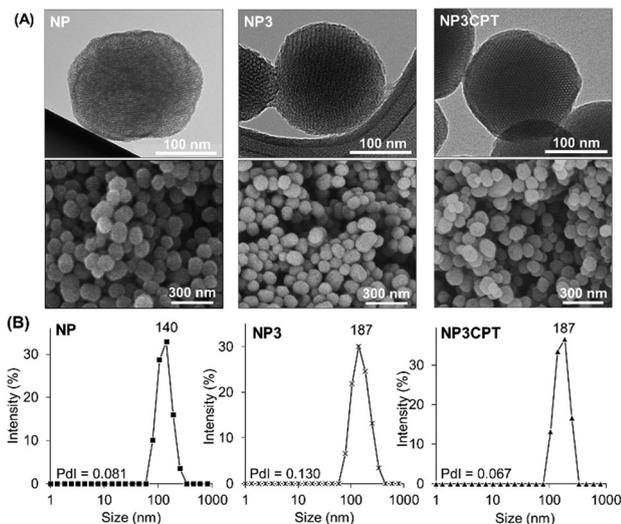
This journal is © The Royal Society of Chemistry 2020

J. Mater. Chem. B, 2020, **8**, 1472–1480 | **1477**

Fig. 7 (A) TEM and SEM images and (B) DLS measurements of **NP**, **NP3** and **NP3CPT**, nanomaterials. The polydispersity indices (PdI, measured by DLS) are included.

polydispersity, consistent with functionalisation of the particles by **Stalk**. The size and low polydispersity of **NP3** remain unchanged after impregnation with CPT (to form **NP3CPT**).

Consequently, the resulting drug loaded **NP3CPT** have a suitable size for nanomedicine applications.

Thereafter, the stability of the **Stalk–Cap** complex as a function of pH (2, 5.5 or 7.4) was investigated in the case of **NP3CPT** by monitoring CPT release in solution *via* UV-Vis absorbance at 380 nm (Fig. 8). The data indicated that only about 5% of the drug is released at neutral pH, confirming that sufficient **Stalk–Cap** bonds remain intact to ensure that the nanoparticles can efficiently transport the chemotherapeutic agents within the blood stream without premature release of the payload.

In contrast, around 38% of CPT was released at pH 5.5 after 24 h. This pH was chosen to mimic that present within the endosomal compartments, and the results suggest that release of the cargo and **Cap** would be expected to occur within the endosomal regions. As expected, essentially quantitative release of **Cap** is observed at pH 2 after only a few hours. This result demonstrates that the removal of the chemotherapeutic **Cap** and subsequent release of the second drug loaded within the pores is controlled by environmental pH. Our earlier studies of the release of **Cap** confirm that its release concentration profile is similar to that of CPT.

In vitro studies on MCF-7 breast cancer cells

Kinetic study. For kinetic studies, MCF-7 cells were incubated at 37 °C for varying time intervals with 40 μg mL^{-1} of **NP3PI**. The nanoparticle internalisation was detected by flow cytometry after co-staining with DAPI to exclude dead cells, and the results presented below represent the averages calculated from three independent experiments. As shown in Fig. 9(A), the internalisation was relatively fast, with 50% of MCF-7 cells containing nanoparticles after 20 h. This result confirmed that
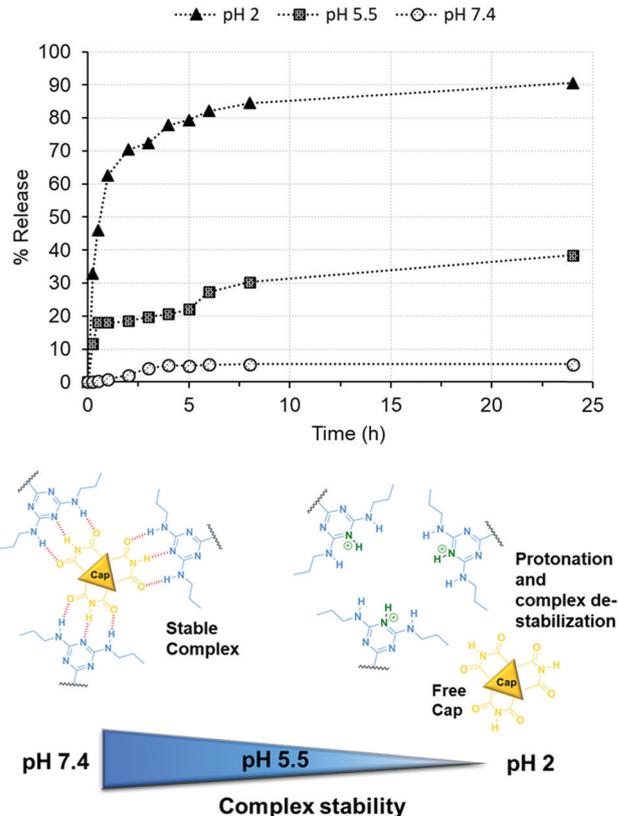

Fig. 8 Release of CPT from **NP3CPT** mesopores (determined by UV/Vis absorbance spectroscopy) as function of pH.

the size and nature of the nanoparticles were suitable for penetrating MCF-7 cancer cells. In addition, it is important to note that, for this measurement, only living cells were considered, and since our cap is biologically active, it might lead to the death of some cells that would be not detected by the approach used here. Hence, the values reported in Fig. 9(A) represent a lower limit for the apparent rate of internalisation.

Uptake of nanoparticles in MCF-7 cells – confocal microscopy

To assess the uptake of nanoparticles in MCF-7 breast cancer cells, the cells were incubated for 20 h with 40 μg mL^{-1} of **NP3RhB** and **NP3PI** (Fig. 9(B)). The endolysosomal compartments were labelled with the green lysotracker and the nuclei marked in blue with the Hoechst stain. The control images correspond to cells that have not been incubated with nanoparticles. In culture cells incubated with **NP3PI**, we can detect the presence of PI in red, and the yellow regions observed in the merged picture demonstrate the co-localisation of **NP3PI** with endo-lysosomal compartments (see yellow arrows in Fig. 9(B)). This validates the internalisation of nanoparticles by the endocytosis pathway. In addition, when culture cells were incubated with nanoparticles loaded with RhB (**NP3RhB**), which is known to cross the cell membranes (and lysosome), we observed that the red dye fully stained the cytoplasm (see white arrows in Fig. 9(B)), confirming the release of the cargo molecules once the nanocarriers have entered the lysosomes. Overall, these

1478 | *J. Mater. Chem. B*, 2020, **8**, 1472–1480

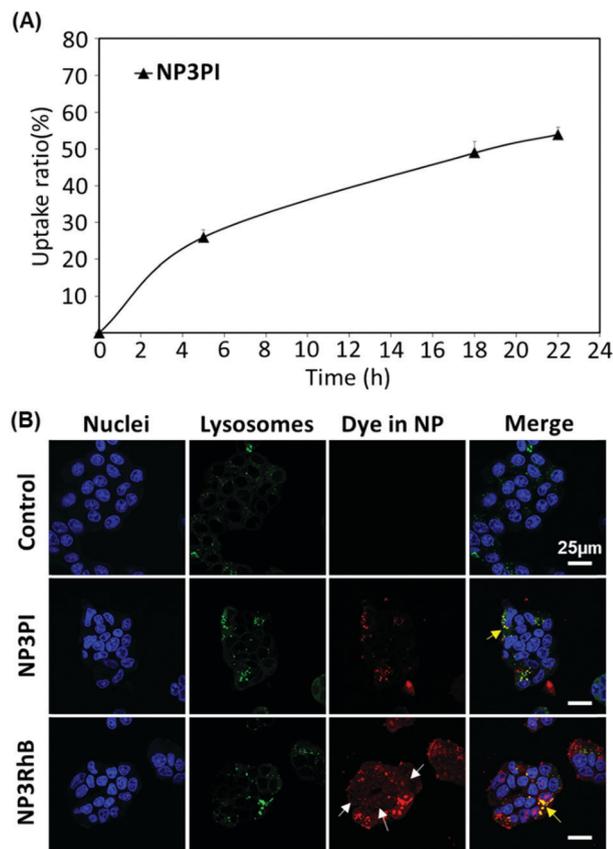This journal is © The Royal Society of Chemistry 2020

Fig. 9 (A) Internalisation rate in MCF-7 cells using **NP3PI**. Error bars show standard deviation. (B) Confocal microscopy of control (top), **NP3PI** (middle) and **NP3RhB** (bottom) after 20 h of incubation in a culture medium of MCF-7 cells.
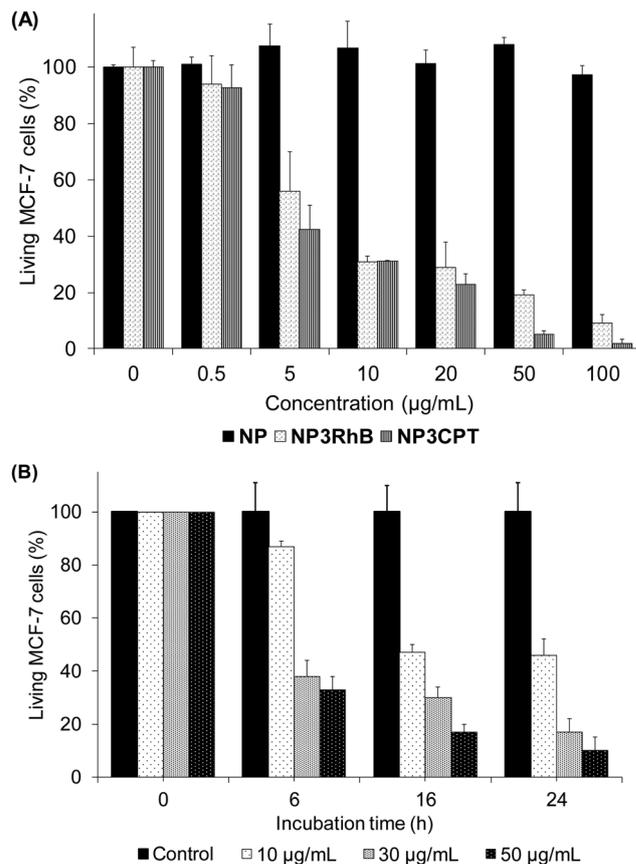

Fig. 10 (A) Cytotoxicity test of **NP**, **NP3RhB** and **NP3CPT** on MCF-7 cells after 72 h of incubation. (B) Cytotoxic effect of **NP3CPT** on MCF-7 as a function of incubation time and concentration. Error bars show standard deviation.

data confirm (1) the uptake of the nanomaterials by the cell *via* the endolysosomal pathway and (2) that the release of active drug molecules is triggered at lysosomal pH, consistent with the pH-sensitivity data included in Fig. 8.

Cytotoxicity

The cytotoxicity of the new nanocarrier on MCF-7 breast cancer cells was then assessed *via* MTT assays. This study was performed with **NP3RhB** to determine the action of the cytotoxic 5-FU cap (RhB is known to be inactive[31]) and with **NP3CPT** to determine if the cytotoxicity is increased by the presence of two different drugs. As shown in Fig. 10(A), which illustrates cell death after 72 h of incubation with different batches of nanoparticles, **NP** exhibited essentially no cytotoxic activity (control). The corresponding data for **NP3RhB** confirmed that the active cap was released, with good cytotoxicity demonstrated against MCF-7 cells. Finally, **NP3CPT** showed excellent tumour elimination, with more than 90% of cell death from a concentration of 50 μg mL^{-1} and up to 99% of cell death at 100 μg mL^{-1}. The IC$_{50}$ of **NP3CPT** under these conditions is 4 μg mL^{-1}, a particularly low value, which demonstrates the complementary and concomitant activity of the multidrug approach employed here, where each drug attacks the cells *via* different and complementary biological pathways.

Following this promising result, the activity of **NP3CPT** on MCF-7 cells was determined at shorter times. For this, incubations with **NP3CPT** at 10, 30 and 50 μg mL^{-1} were performed and followed by MTT assays after 6, 16 and 24 h. The results presented in Fig. 10(B) revealed that the action of **NP3CPT** was relatively fast. Indeed, after only 6 h of incubation, MTT assay results already showed a significant inhibition of cell growth. Moreover, after 24 h the results obtained were close to those observed in the previous study carried out after 72 h of incubation. These data confirm that essentially complete apoptosis of the MCF-7 cells can be achieved, *in vitro*, with the **NP3CPT** system within 24 h.

Conclusions

Herein, a silica-based nanocarrier system in which CPT was loaded within the pores and a 5-FU analogue complexed on the surface as a pore-capping agent has been shown to be a viable system for environmentally-triggered, sequential release of these anti-cancer drugs for successful eradication of breast cancer cells. The nanosystem has been shown to respond to changes in environmental pH, thus enabling the delivery of a multi-drug payload within the lysosomal compartment of cancer cells. In contrast, almost no release of the cytotoxic

This journal is © The Royal Society of Chemistry 2020

J. Mater. Chem. B, 2020, **8**, 1472–1480 | **1479**

compounds was observed under normal physiological conditions, thus minimising toxic side-effects in normal tissue and within the blood stream.

The efficacy of this approach was demonstrated through *in vitro* trials, involving the consecutive delivery of the 5-FU derivative (rapid release) and CPT (diffusion-limited release) in MCF-7 breast cancer cells.

Under the conditions used in this study, essentially complete breast cancer cell apoptosis was observed within 72 h. This result highlights the attractive synergistic effect of the two drugs acting in tandem against tumoral cells. Additionally, the loading of the two synergistic drugs into silica nanocarriers offers the significant advantage of preventing the debilitating side effects usually associated with combination cancer therapy.

It is envisaged that the approach developed in this work could also be extended to multi-combinatorial therapy, involving the sequential release of three or more drugs.

Conflicts of interest

There are no conflicts to declare.

Acknowledgements

Notes and references

1 Q. Hu, W. Sun, C. Wang and Z. Gu, *Adv. Drug Delivery Rev.*, 2016, **98**, 19–34.

2 R. Bayat Mokhtari, T. S. Homayouni, N. Baluch, E. Morgatskaya, S. Kumar, B. Das and H. Yeger, *Oncotarget*, 2017, **8**, 38022–38043.

3 P. Sharma and James P. Allison, *Cell*, 2015, **161**, 205–214.

4 O. C. Farokhzad and R. Langer, *Adv. Drug Delivery Rev.*, 2006, **58**, 1456–1459.

5 N. Kolishetti, S. Dhar, P. M. Valencia, L. Q. Lin, R. Karnik, S. J. Lippard, R. Langer and O. C. Farokhzad, *Proc. Natl. Acad. Sci. U. S. A.*, 2010, **107**, 17939–17944.

6 A. Jhaveri, P. Deshpande and V. Torchilin, *J. Controlled Release*, 2014, **190**, 352–370.

7 J. K. Patra, G. Das, L. F. Fraceto, E. V. R. Campos, M. d. P. Rodriguez-Torres, L. S. Acosta-Torres, L. A. Diaz-Torres, R. Grillo, M. K. Swamy, S. Sharma, S. Habtemariam and H.-S. Shin, *J. Nanobiotechnol.*, 2018, **16**, 71.

8 R. K. Singh, J. C. Knowles and H.-W. Kim, *J. Tissue Eng.*, 2019, **10**, 2041731419877528.

9 I. I. Slowing, B. G. Trewyn, S. Giri and V. S.-Y. Lin, *Adv. Funct. Mater.*, 2007, **17**, 1225–1236.

10 I. I. Slowing, J. L. Vivero-Escoto, C.-W. Wu and V. S. Y. Lin, *Adv. Drug Delivery Rev.*, 2008, **60**, 1278–1288.

11 J. M. Rosenholm, V. Mamaeva, C. Sahlgren and M. Lindén, *Nanomedicine*, 2012, **7**, 111–120.

12 Y. Wang, Q. Zhao, N. Han, L. Bai, J. Li, J. Liu, E. Che, L. Hu, Q. Zhang, T. Jiang and S. Wang, *Nanomedicine*, 2015, **11**, 313–327.

13 J. Wen, K. Yang, F. Liu, H. Li, Y. Xu and S. Sun, *Chem. Soc. Rev.*, 2017, **46**, 6024–6045.

14 M. Vallet-Regí, F. Balas and D. Arcos, *Angew. Chem., Int. Ed.*, 2007, **46**, 7548–7558.

15 C.-H. Lee, S.-H. Cheng, I.-P. Huang, J. S. Souris, C.-S. Yang, C.-Y. Mou and L.-W. Lo, *Angew. Chem., Int. Ed.*, 2010, **49**, 8214–8219.

16 L. Yuan, Q. Tang, D. Yang, J. Z. Zhang, F. Zhang and J. Hu, *J. Phys. Chem. C*, 2011, **115**, 9926–9932.

17 C. Théron, A. Gallud, S. Giret, M. Maynadier, D. Grégoire, P. Puche, E. Jacquet, G. Pop, O. Sgarbura, V. Bellet, U. Hibner, J. I. Zink, M. Garcia, M. Wong Chi Man, C. Carcel and M. Gary-Bobo, *RSC Adv.*, 2015, **5**, 64932–64936.

18 Q. Zhang, F. Liu, K. T. Nguyen, X. Ma, X. Wang, B. Xing and Y. Zhao, *Adv. Funct. Mater.*, 2012, **22**, 5144–5156.

19 A. Rahikkala, S. A. P. Pereira, P. Figueiredo, M. L. C. Passos, A. R. T. S. Araújo, M. L. M. F. S. Saraiva and H. A. Santos, *Adv. Biosyst.*, 2018, **2**, 1800020.

20 Z.-Y. Li, Y. Liu, X.-Q. Wang, L.-H. Liu, J.-J. Hu, G.-F. Luo, W.-H. Chen, L. Rong and X.-Z. Zhang, *ACS Appl. Mater. Interfaces*, 2013, **5**, 7995–8001.

21 F. Muhammad, M. Guo, A. Wang, J. Zhao, W. Qi, Y. Guo and G. Zhu, *J. Colloid Interface Sci.*, 2014, **434**, 1–8.

22 M. C. Llinàs, G. Martínez-Edo, A. Cascante, I. Porcar, S. Borrós and D. Sánchez-García, *Drug Delivery*, 2018, **25**, 1137–1146.

23 S. Giret, C. Théron, A. Gallud, M. Maynadier, M. Gary-Bobo, M. Garcia, M. Wong Chi Man and C. Carcel, *Chem. – Eur. J.*, 2013, **19**, 12806–12814.

24 L. F. Liu, S. D. Desai, T.-K. Li, Y. Mao, M. E. I. Sun and S.-P. Sim, *Ann. N. Y. Acad. Sci.*, 2000, **922**, 1–10.

25 D. B. Longley, D. P. Harkin and P. G. Johnston, *Nat. Rev. Cancer*, 2003, **3**, 330–338.

26 S. Guichard, I. Hennebelle, R. Bugat and P. Canal, *Biochem. Pharmacol.*, 1998, **55**, 667–676.

27 Q. Luo, P. Wang, Y. Miao, H. He and X. Tang, *Carbohydr. Polym.*, 2012, **87**, 2642–2647.

28 C. Théron, A. Birault, M. Bernhardt, L. M. A. Ali, C. Nguyen, M. Gary-Bobo, J. R. Bartlett, M. Wong Chi Man and C. Carcel, *J. Sol-Gel Sci. Technol.*, 2019, **89**, 45–55.

29 M. K. Trivedi, R. M. Tallapragada, A. Branton, D. Trivedi, G. Nayak, R. K. Mishra and S. Jana, *J. Mol. Pharm. Org. Process Res.*, 2015, **3**, 128–134.

30 M. A. Mondragón, V. M. J. Castaño, M. C. A. Garcia and S. Téllez, *Vib. Spectrosc.*, 1995, **9**, 293–304.

31 P. Fisher, *Wildl. Soc. Bull.*, 1999, **27**, 318–329.

1480 | *J. Mater. Chem. B*, 2020, **8**, 1472–1480

This journal is © The Royal Society of Chemistry 2020